The Impact of Stacking and Phonon Environment on Energy Transfer in Organic Chromophores: Computational Insights

Aliya Mukazhanova,[1] Hassiel Negrin-Yuvero[2], Victor M. Freixas,[2] Sergei Tretiak,[3] Sebastian Fernandez-Alberti,[2] Sahar Sharifzadeh[1,4]

[1] Division of Materials Science and Engineering, Boston University, USA
[2]Universidad Nacional de Quilmes/CONICET, Argentina
[3] Theoretical Division and Center for Integrated Nanotechnologies, Los Alamos National Laboratory, USA
[4] Department of Electrical and Computer Engineering, Boston University, USA

ABSTRACT

Energy transfer in organic materials is extensively studied due to many applications in optoelectronics. The electronic and vibrational relaxations within molecular assemblies can be influenced by stacking arrangements or additions of a backbone that unites them. Here, we present the computational study of the photoexcitation dynamics of a perylene diimide monomer, and face-to-face stacked dimer and trimer. By using non-adiabatic excited-state molecular dynamics simulations, we show that the non-radiative relaxation is accelerated with the number of stacked molecules. This effect is explained by differences in the energy splitting between states that impacts their corresponding nonadiabatic couplings. Additionally, our analysis of the vibronic dynamics reveals that the passage through the different conical intersections that participate in the relaxation of the stacked systems, activate a positive feedback mechanism. This effect involves a narrow set of vibrational normal modes that accelerate the process by increasing the efficiency of its vibronic dynamics. In contrast, an addition of a biologically inspired backbone slows down the relaxation rate due to its participation in the vibronic dynamics of the molecular stacking arrangements. Our results suggest the stacking arrangements and common backbones as strategies to modulate the efficiency of electronic and vibrational relaxation of diimide-based systems and other molecular aggregates.

INTRODUCTION

Energy transfer in organic materials has received extensive attention due to its importance to solar energy conversion; i.e. organic solar cells, and natural and artificial photosynthesis.[1–7] This process involve directed migration of electronic excitations (excitons) leading to energy funneling. Organic chromophores efficiently absorb solar energy, which can then be directed to a reaction center in order to be transformed into chemical energy or converted into free charge carriers to generate current. In both cases, the photoconversion efficiency depends on the relative rates associated with energy transfer and radiative decay.[8,9] To understand and control these processes for the design of new more efficient materials, it is necessary to understand the relaxation pathways for the excited states involved.

One approach for tuning the energy flow and decay of optical excitations in organic materials is through the design of aggregation.[10–13] For example, stacking organic chromophores can lead to energy flow over long distances by increasing radiative lifetime, through inter-molecular electronic couplings.[12,13] Additionally, in both natural and artificial photosynthetic

systems, inter-molecular electronic and vibrational (vibronic) coherences can lead to efficient energy transfer and conversion.[14–17] For these systems, the vibrations of the protein environment (phonon bath) significantly impacts the evolution of these coherences.[14] This coupling of electronic excitations with nuclear motions in organic materials is a complex phenomenon that is not well-understood. Photoexcitation typically results in a simultaneous excitation of electrons and nuclei, known as a vibronic state.[18,19] Subsequently, during internal conversion generally occurring on less than 1 picosecond[20]), energy unidirectionally flows from electronic to vibrational degrees of freedom (non-radiative relaxation), with the electrons and nuclei trending towards the lowest point of the excited-state potential energy surface.[21,22] The lifetime and migration of the excess of electronic and vibrational energy in the excited states then determines its efficiency in solar energy conversion. Other relaxation processes such as intersystem crossings and radiative decays may have much longer timescales and typically occur over several nanonoseconds or longer.[53] Spectroscopically, the time-scales associated with internal energy conversion can be extracted from time-resolved spectroscopy. Understanding the atomistic behavior of these relaxation pathways can lead to proposing new chemical structures or intermolecular arrangements to control them, improving the design of solar energy conversion materials.[2,23]

In this study, we combine density functional theory (DFT) and non-adiabatic excited state dynamics simulations to study molecular systems composed of one to three perylene-3,4,9,10-tetracarboxylic diimide (PDI) chromophores with and without a biologically inspired backbone as an ideal model system to understand complex relationships between structure and photoexcited vibronic dynamics (see Figure 1). Stacked PDI derivatives are a promising example of molecular assembly with strong π-π interactions featuring favorable optical absorption and self-assembly properties.[24–27] Due to the widespread interest in the properties and applications of PDIs, there are extensive investigations of their optical properties[28–36] but a limited number of excited state dynamics studies[11,37–39] including our previous works.[40,41]

Previously, we studied the role of dimerization on energy decay within PDIs,[40] and analyzed which vibrational modes assist energy transfer in a PDI monomer with and without addition of an alkyl functional group.[41] In this work, we characterize the role of stacking and the "phonons" of the biologically-inspired backbone during the internal conversion process using atomistic non-adiabatic excited-state molecular dynamics (NEXMD) simulations.[42] We find that stacking significantly speeds up internal energy conversion dynamics while the backbone slows it down. We attribute the former to the formation of energy split states that can efficiently funnel molecular excitations from the high energy to the lowest excited state involving several vibrational modes that assist non-adiabatic transitions. The latter is due to the restriction of atomic motion due to the backbone. Moreover, we determine that the backbone leads to delocalization of the transition density and modifies the vibrational modes that facilitate transitions between states.

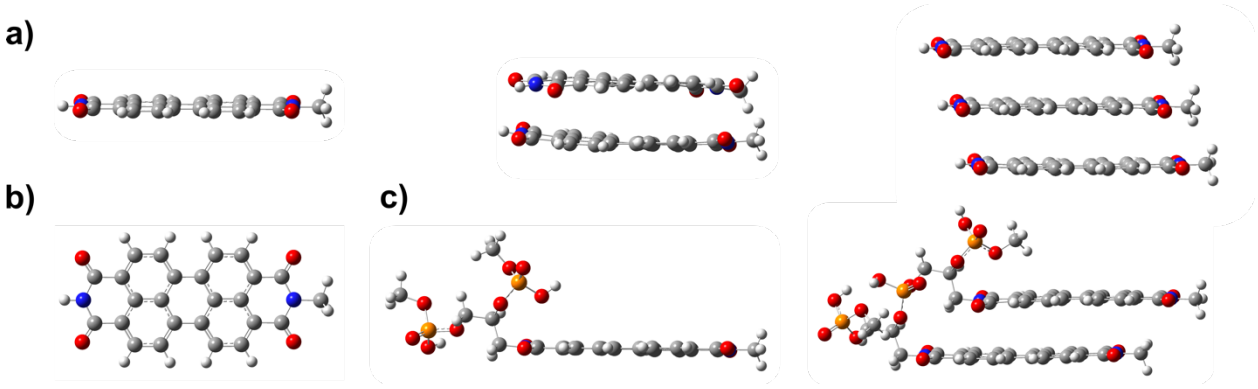

Figure 1. The perylene diimide molecules considered in this work: (a) from left to right: monomer, dimer, trimer; (b) top view of the monomer; (c) from left to right: monomer with backbone, dimer with backbone.

RESULTS

A. The Role of Stacking

We first analyze the optical absorbance spectra associated with the low energy excited states of the monomer, dimer, and trimer of PDI obtained using NEXMD package (see Computational Methods Section). We note that, due to ground state classical MD simulations, summation over the snapshots does not resolve the vibronic progression of absorbance, which would require an explicit consideration of Huang-Rhys factors. As shown in Figure 2, the first singlet excited state of the monomer (S_1), the second excited state (S_2) of the dimer, and the third excited state (S_3) of trimer are optically allowed (bright), while most other excited states are weakly absorbing or optically forbidden (dark). This finding is in a qualitative agreement with TDDFT calculations within the wB97-XD functional though the transition energies of excited states differ (see Figure S4).

Our results are also consistent with the Frenkel exciton model of an H-like aggregate.[43] The Frenkel exciton Hamiltonian for dimer and trimer systems can be written as

$$H_2 = \begin{pmatrix} E & V \\ V & E \end{pmatrix}, \qquad (1a)$$

$$H_3 = \begin{pmatrix} E & V_1 & V_2 \\ V_1 & E & V_1 \\ V_2 & V_1 & E \end{pmatrix}, \quad (1b)$$

For the dimer, E is the energy of the S_1 state for each monomer, V is the corresponding coupling between both parallel monomers (Eq. 1a). For the trimer, E is the energy of the S_1 state for each monomer, V_1 is the coupling between adjacent monomers, and V_2 is the coupling between the top and bottom monomers (Eq. 1b). For a dimer with two identical monomers stacked in a parallel orientation, this model would indicate that S_2 state has a significant oscillator strength while S_1 is dark,[19] which is consistent with our findings. For a trimer of parallel-stacked molecules, a bright S_3 state can be similarly rationalized. The eigenvectors corresponding to the two lowest

energy excited states (S_1 and S_2) of the total system are a result of excitations on each monomer with misaligned transition dipole moments, which will result in a low oscillator strength. For S_3 however, the transition dipole moments of all three molecules are aligned, resulting in a brighter state. More details on the electronic transition density localization and relative oscillator strengths of each state of the monomer, dimer and trimer and their agreements with eigenvalues and eigenvectors predicted by the Frenkel exciton model for the dimer and trimer can be found in SI Sections 1 and 2.

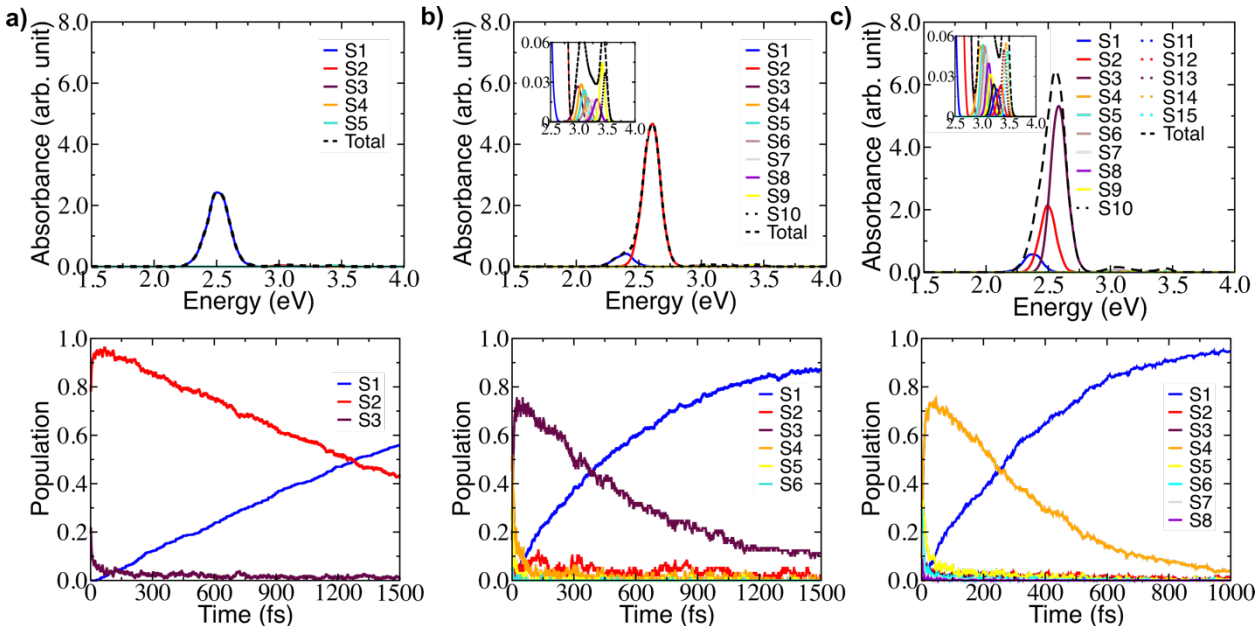

Figure 2. Absorption spectrum and excited-state population analysis for the perylene diimide (a) monomer (b) dimer, and (c) trimer.

We next discuss non-radiative relaxation dynamics obtained using non-adiabatic molecular dynamics simulations with NEXMD package. There is a significant stacking dependence to the calculated internal excited-state energy conversion timescales of the molecules as summarized in the lower row of Figure 2. For the monomer (Figure 2a), internal conversion leads to 50% population transfer from S_2 to S_1 at 1.3 ps. Stacking speeds up internal energy conversion significantly. For the dimer, the laser pulse initially partially occupies S_3 (20.2%), S_4 (45.6%), S_5 (30%), and S_6 (4.2%); the population rapidly transfers (within a few fs) to S_3 with subsequent, slower decay from S_3 to S_1. There is 50% population transfer to S_1 at 400 fs (Figure 2b). For the trimer, there is initial partial occupation of the S_5 (32.7%), S_6 (32.7%), S_7 (20%), S_4 (9.2%), S_8 (5.4%) that rapidly transfers (within a few fs) to S_4, with a slower decay from S_4 to S_1. There is 50% population transfer from S_4 to S_1 at about 240 fs. Thus, we find that an increase in the number of stacked molecules noticeably accelerates the energy decay.

Assuming a sequential character of the decay (i.e. $S_3 \rightarrow S_2 \rightarrow S_1$), the enhancement of internal energy conversion in stacked molecules can be understood as a consequence of the energy splitting that can be readily rationalized withing the context of Frenkel exciton model, which makes consecutive states to be energetically close-spaced. Since the non-adiabatic coupling is inversely proportional to energy gap, the splitting effectively contributes to a faster decay. The

monomer's $S_2 - S_1$ energy gap is 0.52 eV, the dimer's $S_3 - S_2$ and $S_2 - S_1$ splittings are 0.37 eV and 0.2 eV, respectively, and the trimer's $S_4 - S_3$, $S_3 - S_2$ and $S_2 - S_1$ gaps are 0.38 eV, 0.1 eV, 0.12 eV, respectively (see Tables S1 and S2 for excited-state energies). This effect is demonstrated by the non-adiabatic coupling terms (NACT) shown in Figure S5. Here the averaged absolute value of the non-adiabatic coupling term between S_1 and S_2, NACT(1,2) increases with stacking: it attains the highest and the lowest values for the trimer and the monomer, respectively. Nevertheless, while energy differences can partially explain changes in the relaxation times between monomer and dimer and trimer, NACTs also depend on the effective overlap of excited states and nuclear velocities.[44]

Table 1. Dimer and Trimer Normal modes with the highest overlap values with respect to $\boldsymbol{d}_{12}^{SVD,1}$ and $\boldsymbol{d}_{23}^{SVD,1}$ associated to the corresponding $S_2 \rightarrow S_1$, $S_3 \rightarrow S_2$ and $S_4 \rightarrow S_3$ electronic transfers. Frequencies (cm^{-1}) are given in parenthesis.

Dimer				Trimer					
$S_2 \rightarrow S_1$		$S_3 \rightarrow S_2$		$S_2 \rightarrow S_1$		$S_3 \rightarrow S_2$		$S_4 \rightarrow S_3$	
Mode # (Freq.)	Overlap	Mode # (Freq.)	Overlap	Mode # (Freq.)	Overlap	Mode # (Freq.)	Overlap	Mode # (Freq.)	Overlap
226 (1865)	0.88	226 (1865)	0.78	256 (1402)	0.53	256 (1402)	0.51	259 (1410)	0.45
223 (1795)	0.16	209 (1693)	0.27	265 (1431)	0.39	265 (1431)	0.40	325 (1763)	0.38
222 (1792)	0.16	207 (1679)	0.25	316 (1719)	0.38	316 (1719)	0.37	257 (1408)	0.37
207 (1679)	0.14	222 (1792)	0.14	258 (1408)	0.31	259 (1410)	0.33	265 (1431)	0.32
225 (1797)	0.12	199 (1596)	0.13	259 (1410)	0.31	258 (1408)	0.31	262 (1419)	0.25
122 (908)	0.10	223 (1795)	0.13	310 (1647)	0.18	310 (1647)	0.18	264 (1428)	0.16
121 (904)	0.10	122 (908)	0.11	274 (1480)	0.17	274 (1480)	0.18	261 (1418)	0.16
209 (1693)	0.10	175 (1416)	0.10	271 (1476)	0.11	261 (1418)	0.12	294 (1580)	0.15
224 (1795)	0.09	121 (904)	0.10	261 (1418)	0.10	271 (1476)	0.11	286 (1524)	0.14
234 (2025)	0.08	234 (2025)	0.09	264 (1428)	0.10	287 (1525)	0.09	244 (1335)	0.13

To better understand the energy transfer pathways and the sequence of decay, we analyze the non-adiabatic derivative couplings between two states *i* and *j*, $\boldsymbol{d}_{ij}$, for the trajectory ensemble. These quantities are directly responsible for non-radiative transitions between electronic states. In the previous article,[41] we have shown that, for the PDI monomer, $\boldsymbol{d}_{12}^{SVD,1}$ computed via the Singular Value Decomposition (SVD) provides a good representation of the set of the originals $\boldsymbol{d}_{12}$ (i.e., at the moment of effective $S_2 \rightarrow S_1$ transition at each trajectory). This indicates that a single pathway can well describe the atomic motions that facilitate energy transitions for all trajectories. Herein, an equivalent analysis has been applied for the dimer and trimer. For the PDI dimer, average values of 0.95 +/- 0.05 and 0.6 +/- 0.28 are obtained for the projection of $\boldsymbol{d}_{12}^{SVD,1}$ and $\boldsymbol{d}_{23}^{SVD,1}$ with the original $\boldsymbol{d}_{12}$ and $\boldsymbol{d}_{23}$ ensembles. The high projection value indicates that the effective $S_2 \rightarrow S_1$

transition evolves through a single energy-transfer pathway along their corresponding direction of $\boldsymbol{d}_{12}^{SVD,1}$. The $S_3 \rightarrow S_2$ involves more than one pathway with the dominant one being in the direction of $\boldsymbol{d}_{23}^{SVD,1}$. For the PDI trimer, average values of 0.77 +/- 0.20, 0.80 +/- 0.16 and 0.47 +/- 0.27 are obtained for the projection of $\boldsymbol{d}_{12}^{SVD,1}$, $\boldsymbol{d}_{23}^{SVD,1}$ and $\boldsymbol{d}_{34}^{SVD,1}$ onto the respective $\boldsymbol{d}_{12}$, $\boldsymbol{d}_{23}$ and $\boldsymbol{d}_{34}$ ensembles. This indicates that, while $S_4 \rightarrow S_3$ involves more than one relaxation pathway, $S_3 \rightarrow S_2$ and $S_2 \rightarrow S_1$ transitions are funneled through single ones. The efficiency of this effect modulates the transient nuclear velocities that ultimately lead to similar NACT(1,2) for the dimer and trimer (see Figure S5) despite differences $S_2 - S_1$ energy gaps and different NACT(2,3) values despite similar $S_3 - S_2$ energy gaps.

To further resolve the energy transfer process, Table 1 summarizes the projections of $\boldsymbol{d}_{23}^{SVD,1}$ and $\boldsymbol{d}_{12}^{SVD,1}$ vectors onto the basis of the equilibrium normal modes (ENMs) (see Eq. 5 in Computational Methods). For the monomer, we previously showed that the effective atomic vibrations that assist the $S_2 \rightarrow S_1$ transfer correspond to a selected subset of modes within the range of 1770−1800 cm^{-1}.[41] Similarly, only a few normal modes of the dimer significantly overlap with the $\boldsymbol{d}_{ij}^{SVD,1}$. The set of these *active* modes are equivalent for both $S_3 \rightarrow S_2$ and $S_2 \rightarrow S_1$ transitions, being mode #226 (represented in Figure S6) the one with the highest overlap with $\boldsymbol{d}_{12}^{SVD,1}$ and $\boldsymbol{d}_{23}^{SVD,1}$ directions, and therefore, being the vibrational excitation that most strongly assists in internal energy conversion.

A further inspection of this issue can be performed by monitoring the average vibrational energy as a function of delay time, $\tau = t - t_{hop}$, relative to the moment of non-adiabatic $S_3 \rightarrow S_2$ and $S_2 \rightarrow S_1$ transitions for common modes with dominant contributions of the corresponding $\boldsymbol{d}_{23}^{SVD,1}$ and $\boldsymbol{d}_{12}^{SVD,1}$ directions (see Figure 3). We determine that these modes are activated after both transfers. In particular, mode #226 remains activated for longer times after the $S_3 \rightarrow S_2$ transfer with respect to $S_2 \rightarrow S_1$ counterpart. This explains why S_2 does not transiently accumulate population during the electronic relaxation from the S_3 state to the S_1 state (see Figure 2b): the $S_3 \rightarrow S_2$ transition activates vibrations that are also in the direction of the $S_2 \rightarrow S_1$ transition, inducing a more efficient and faster terminal transfer to the S_1 state. Stated differently, the evolution from $S_3 \rightarrow S_2$ activates a positive feedback mechanism that involves a common set of vibrational normal modes that accelerate the $S_2 \rightarrow S_1$ relaxation.

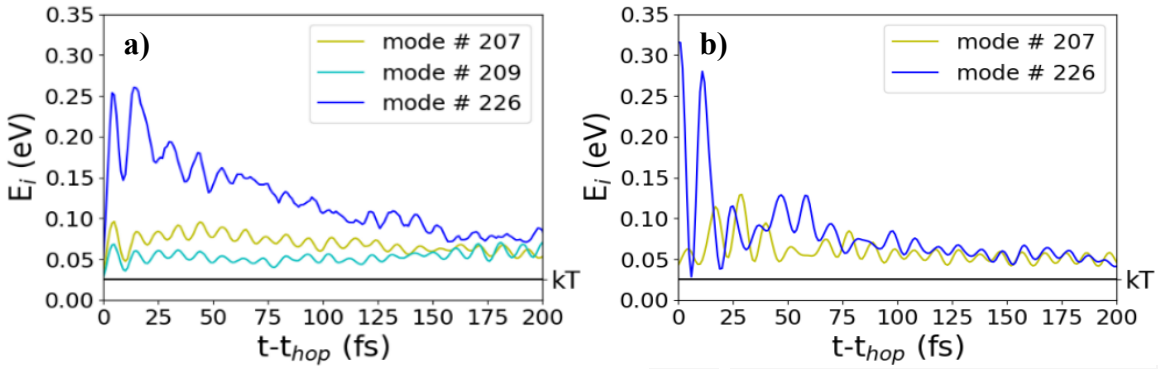

Figure 3. Average vibrational energies of the dimer $E_i(\tau)$ as a function of delay time, $\tau = t - t_{hop}$, relative to the moment of non-adiabatic (a) $S_3 \rightarrow S_2$ and (b) $S_2 \rightarrow S_1$ transitions for common modes with dominant contributions to the corresponding $\boldsymbol{d}_{23}^{SVD,1}$ and $\boldsymbol{d}_{12}^{SVD,1}$ directions.

Table 1 also shows the projection of the different $\boldsymbol{d}_{ij}^{SVD,1}$ onto the basis of ENMs for the PDI trimer. The $S_3 \rightarrow S_2$ and $S_2 \rightarrow S_1$ transitions share the five normal modes that contribute the most to $\boldsymbol{d}_{23}^{SVD,1}$and $\boldsymbol{d}_{12}^{SVD,1}$ directions respectively (modes #256, #265, # 316, #259 and #258 in Figure S7). For the $S_4 \rightarrow S_3$ transition, normal modes at 1431 cm^{-1} and 1410 cm^{-1} (#265 and #259) have a significant participation as well as a quasi-degenerate mode (#257, 1408 cm^{-1}) with #258 that participates in the $S_3 \rightarrow S_2$ and $S_2 \rightarrow S_1$ transitions, involving equivalent nuclear motions for at least one of the units. This is also observed by comparing mode #316 (1719 cm^{-1}) (involved in the $S_3 \rightarrow S_2$ and $S_2 \rightarrow S_1$ transitions) and #325 (1763 cm^{-1}) (involved in the $S_4 \rightarrow S_3$ transition). At this point it is important to mention that resonance conditions identified by ENM frequencies should be considered as an approximation and are subjected to changes due to vibrational anharmonicities and vibronic couplings. An alternative approach, but computationally more expensive, is calculation of Instantaneous Normal Modes (INM). Differences in frequencies ~44 cm^{-1}, like it is the case for mode #316 (1719 cm^{-1}) and #325 (1763 cm^{-1}), are within the expected values of standard deviations of INM frequencies fluctuations due to changing curvature of excited state potential energy surface. Moreover, these modes involve equivalent *intra-monomer* nuclear motions, as can be seen in Figure S7.

Thus, as with the dimer, the overall sequential $S_4 \rightarrow S_1$ relaxation pathway involves a common bundle of states that leads to no transient accumulation of electronic populations in the intermediate S_3 and S_2 states, as shown in Figure 2c). Nevertheless, the normal modes involved in the $S_3 \rightarrow S_2$ and $S_2 \rightarrow S_1$ transitions during PDI trimer simulations are not equivalent to the corresponding modes in the PDI dimer. That is, the different interactions between monomers modulate the normal modes of the total system.

Vibronic dynamics condition transient localization or delocalization of the exciton due to stacking. In order to analyze this point, we study the change in $(p^{g\alpha})_X^2$ (see Eq. 3 in Computational Methods Section) as a function of time for the ensemble of trajectories, shown in Figure 4a). In the case of dimer, values of $(p^{g\alpha})_X^2 \sim 0.5$ indicate delocalization over both monomers while $(p^{g\alpha})_X^2 \sim 0$ or 1 indicate localization on one of the monomers. Initially 76% of trajectories present $(p^{g\alpha})_X^2$ values that indicate the exciton localization in one of the monomers, i.e. $0 < (p^{g\alpha})_X^2 < 0.2$ or $0.8 < (p^{g\alpha})_X^2 < 1$ (see Figure S8). There are persistent oscillations of the transition density (TD) from one monomer to another and a small probability of delocalization throughout simulation time. Subsequently, the TD becomes more localized and 96% of trajectories present values of $0 < (p^{g\alpha})_X^2 < 0.2$ or $0.8 < (p^{g\alpha})_X^2 < 1$.

Our analysis of the localization/delocalization of $(p^{g\alpha})_X^2$ among the three molecules of the trimer (see Figure S9), reveals that the excited state starts out somewhat delocalized, with around 80% delocalized over more than one monomer. During the excited state dynamics, the TD localizes slightly over time but there are a significant number of trajectories that remain delocalized over three monomers. Most of trajectories show predominant delocalization on two monomers, while 39% of the trajectories show delocalization over all three monomers ($0.2 < (p^{g\alpha})_X^2 < 0.8$) even after 1 ps. These results indicate that stacking leads to a more sustained delocalization of the exciton, which is less perturbed by coupling to atomic vibrations.

B. The Role of Backbone

In naturally occurring organic systems, an environment of chromophores has a significant impact on exciton dynamics including coherence and transfer.[45] To understand the role of a

tethering environment on the excitonic properties, we study the PDI monomer and dimer on a biologically inspired backbone, which has been synthesized previously, and studied by some of us.[32] The resulting absorption spectrum and population dynamics are shown in Figure 4. In the case of the monomer, no significant changes in the absorption spectrum lineshape and oscillator strength are detected upon addition of the backbone (Figure 4a). However, the backbone blue-shifts the absorption spectrum of the dimer, narrows the peaks and increases the intensity of the bright S_2 peak (Figure 4b). This is because the backbone influences the intermonomer displacements, and, as a consequence, changes the lineshape and blue-shifts the absorption spectrum. This is illustrated in Figure S10, in which the backbone is removed but the displacement between monomers is maintained. The resulting absorption spectrum is almost identical to the dimer with backbone.

Interestingly, despite the fact that the backbone does not significantly impact the absorption spectrum and energy spacing of the monomer, it slows down the decay (Figure 4c); 50% population transfer from S_2 to S_1 happens at more than 1.5 ps as compared with 1.3 ps without the backbone. The slowdown of the decay is much more pronounced for the dimer. The 50% decay time is increased by almost a factor of 3 to 1.5 ps in the system with backbone. This slowdown in dynamics can be seen in the averaged absolute values of the NACTs (Figures S11 and S12). For the monomer, the NACT(1,2) is similar for the systems with and without backbone whereas NACT(1,3) is slightly reduced with the addition of a backbone (Figure S11). For the dimer, the impact of a backbone is much more significant for NACT(1,2) and NACT(2,3) because there are fewer high-value coupling terms over time when the backbone is present. This is particularly clear for the NACT(1,2) within the first 400 fs of the trajectory (Figure S12).

To better understand the role of backbone on energy conversion, we consider population dynamics for the dimer without backbone but keeping the initial inter-molecular orientation of the system with the backbone (Figure S13). The observed population dynamics in this system is similar to that in the dimer without backbone, indicating that the presence of the backbone contributes more than just modification of the inter-molecular geometry. Thus, we expect that the slowdown of dynamics of the dimer with backbone is due to the participation of the backbone on the vibronic dynamics of the dimer; in particular, the backbone will restrict the vibrational excitations of the molecules.

Lastly, we consider the role of the backbone on exciton delocalization in the dimer (see Figure S14). A dimer has the TD delocalized over both monomers initially, as opposed to a dimer without backbone. In 99% of the trajectories with the backbone, the TD is initially delocalized over both monomers, and after 50 fs, it becomes slightly localized on one of the monomers. However, there is less pronounced localization of TD on one half of the molecule during simulation time compared to the case with absent backbone. Subsequently, around 900 fs the TD becomes slightly localized and maintains some degree of delocalization up to the end of the simulation at 1 ps. Overall, the exciton delocalization with backbone may be because the backbone hinders the vibrations of the molecules, thus limiting the number of localized vibronic states that can occur.

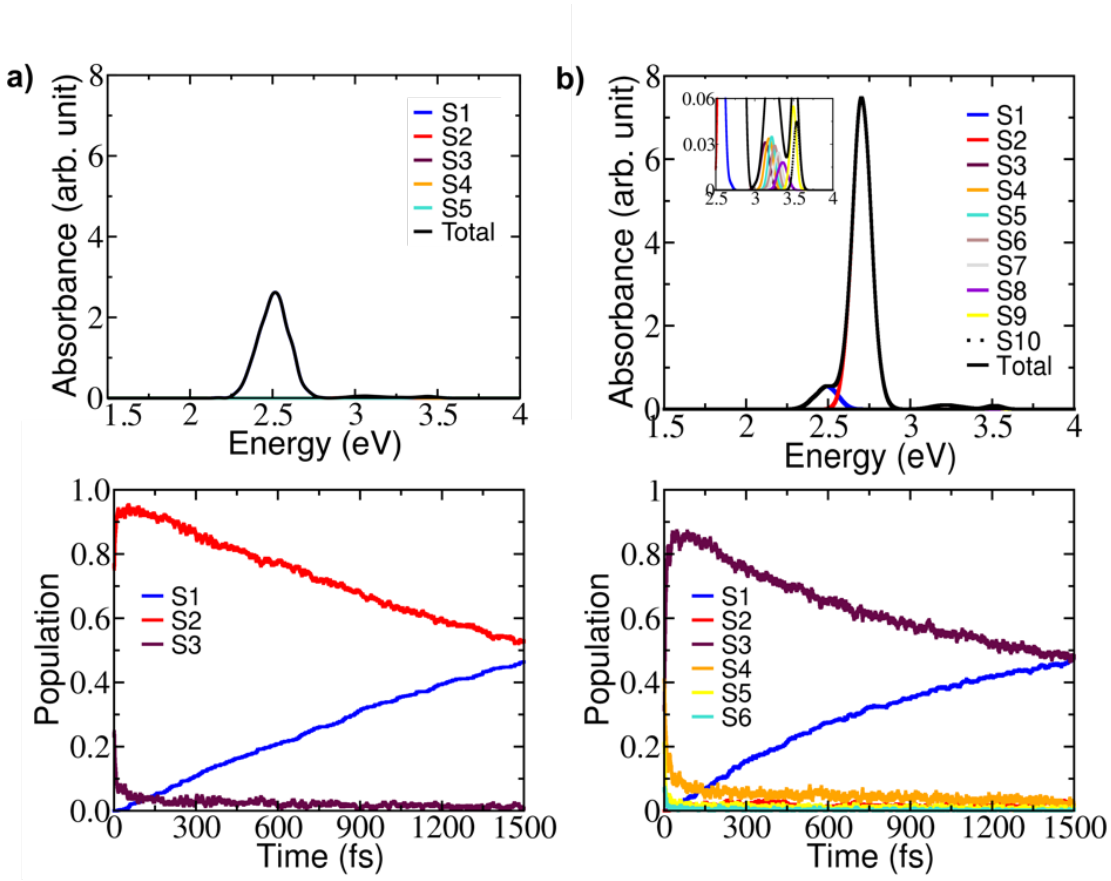

Figure 4. The absorption spectrum and population dynamics of a) monomer with backbone and b) dimer with backbone.

CONCLUSIONS

In summary, we have analyzed the role of stacking, backbone, and vibrational modes on perylene diimide (PDI) stacks serving as a model system to understand energy transfer in organic molecular assemblies. Non-adiabatic excited-state molecular dynamic simulations applied to the PDI monomer, dimer, and trimer deliver a comprehensive atomistic picture of concomitant distinct relaxation processes. In agreement with our previous studies,[40] we find that the stacking speeds up the energy transfer efficiency, such that the relaxation rate is the fastest for trimer, intermediate for dimer and the slowest for monomer. Additionally, by analysis of the vibronic coupling at transition points, we demonstrate that the relaxation pathway dominates by a sequential energy transfer between states. This process activates a positive feedback mechanism involving a common set of vibrational normal modes that accelerate the process by increasing the efficiency of its vibronic dynamics. Moreover, we determine that while the exciton in the dimer is becoming localized on one monomer at ambient conditions, exciton delocalization can persist in the trimer. Lastly, we show that the inclusion of a backbone that bridges the monomers, slows down the relaxation rates and facilitates more delocalized states. These results are suggestive of appearance of the hinderance of vibrational excitations introduced by the steric constraint. Altogether, this

computational study demonstrates a significant modification of mono-molecular non-radiative relaxation dynamics due to intermolecular interactions in the ensemble and introduction of chemical bridges. These effects need to be factorized in when designing functional macromolecular light-harvesting structures mimicking natural photosynthetic systems.

COMPUTATIONAL METHODS

A. Computational protocol

The ground state geometries of the perylene diimide molecules (monomer, dimer and trimer) are initially optimized within density functional theory (DFT) using the wB97-XD[46] exchange-correlation functional and a 6-31G(d) basis set as implemented in the Gaussian 16 package.[47] The wB97-XD functional is chosen because it includes long-range exact exchange for accurate electronic structure and corrections accounting for long-range van der Waals interactions that are necessary for accurate initial geometries. These optimized geometries have a center of mass distances among perylene cores of 3.14 Å for dimer, 4.72 Å for dimer with backbone, 3.65 Å (top and center perylene molecules) and 3.67 Å (center and bottom perylene molecules) for trimer (XYZ coordinates for optimized geometries are provided in Supporting Information). Ground state molecular dynamics (MD) simulations are then performed starting from these DFT-optimized structures by using the AM1[48,49] semi-empirical Hamiltonian as implemented in NEXMD package.[42] In order to account for the missing van der Waals interactions in the Hamiltonian, the distance between the limiting monomers is constrained by fixing the distances between pairs of equivalent nitrogen atoms using the RATTLE algorithm.[50] Ground state MD trajectories are run for 300 ps using the Langevin thermostat set to 300 K with a friction coefficient $\gamma = 20$ ps^{-1} and a time step of 0.5 fs. Configurations equi-spaced in time are then collected for subsequent NEXMD simulations.

Vertical excitation energies and oscillator strengths of each snapshot are computed within the random phase approximation using the semi-empirical AM1 Hamiltonian. For all structures, the first five (ten/fifteen) excited states are considered for the monomer (dimer/trimer). For each molecule, the final absorption spectrum at room temperature is calculated by including a Gaussian broadening of 0.05 eV to the absorption spectra of each snapshot.

The NEXMD simulations are carried out at constant energy. More details on this approach can be found elsewhere.[42] During these simulations constraints on nitrogen atoms are released. A Gaussian shaped laser pulse with energy of 3.02 eV for the monomer and 3.05 eV (3.06 eV) for the dimer (trimer) is applied with a broadening of 0.05 eV. To compare the molecules in a consistent manner, we excite the monomer, dimer, and trimer to the energy of the second (S_2), fourth (S_4), and sixth (S_6) excited-state, respectively, and simulate the decay to the lowest energy excited-state (S_1). In addition, we include higher energy but nearly-degenerate states in the simulation (S_3, S_5/S_6, S_7/S_8 for the monomer, dimer, and trimer, respectively) to allow energy transfer to higher energy states. These additions introduce some differences in the electronic relaxation rates of the monomer and dimer with respect to those reported in our previous work.[40,41]

A total of 700 NEXMD trajectories are calculated for each molecule for 1.5 ps at constant energy with a classical time-step of 0.1 fs (nuclei) and a quantum time-step of 0.025 fs (electrons). Specific treatments of decoherence[51] and trivial unavoided crossings[52] are included in these simulations.

B. Analyses of transient exciton localization and migration.

The spatial exciton delocalization over molecules is calculated by orbital representation of the electronic transition density.

$$(p^{g\alpha})_{nm} \equiv \langle \phi_\alpha(r;R(t)) | c_m^\dagger \, c_n | \phi_g(r;R(t)) \rangle, \qquad (2)$$

where $\phi_g(r;R(t))$ and $\phi_\alpha(r;R(t))$ are wave functions of ground and excited states, and $c_m^\dagger$ (c_n) are the creation (annihilation) operators; and the indices *n* and *m* refer to atomic orbital (AO) basis functions. The diagonal elements $(p^{g\alpha})_{nn}$ represent the change in electronic density upon photoexcitation from ground state (g) to excited state (α). The fraction of transition density on each monomer X is calculated as

$$(p^{g\alpha})_X^2 = \frac{\sum_{n\epsilon X}(p^{g\alpha})_{nn}^2}{\sum_n (p^{g\alpha})_{nn}^2}. \quad (3)$$

C. Vibrational analysis

Representative vectors of non-adiabatic derivative couplings $\boldsymbol{d}_{ij}$ for the ensemble of NEXMD simulations are analyzed using the Singular Value Decomposition (SVD) of the matrix $\boldsymbol{A}$ of dimension $3N \times K$. Here N is the number of nuclear degrees of freedom and *K* is the number of NEXMD simulations featuring an effective $S_j \rightarrow S_i$ transition. An effective $S_j \rightarrow S_i$ transition is defined as the last $S_j \rightarrow S_i$ transition without subsequent $S_i \rightarrow S_j$ back-hopping during the rest of the simulation. Matrix $\boldsymbol{A}$ is built with columns representing the $\boldsymbol{d}_{ij}$, at the moment of effective $S_j \rightarrow S_i$ transition in each of the *K* NEXMD trajectories. Thereafter, the SVD is performed as

$$\mathbf{A} = \mathbf{U} \cdot \mathbf{W} \cdot \mathbf{V}^T, \qquad (4)$$

where $\boldsymbol{U}$ is a 3*N*x*K* column-orthogonal matrix, and $\boldsymbol{V}$ and $\boldsymbol{W}$ are *K*x*K* diagonal and orthogonal matrices respectively. We denote $\boldsymbol{d}_{ji}^{SVD,k}$ as the kth column of the matrix $\boldsymbol{U}$ with the associated largest value of w_k. The $\boldsymbol{d}_{ij}^{SVD,k}$ vector or vectors with the largest w_k can then be considered as representative of the ensemble of $\boldsymbol{d}_{ij}$ collected from the different NEXMD simulations.

The $\boldsymbol{d}_{ij}^{SVD,k}$ vectors can be further projected onto the equilibrium normal mode (ENM) basis set evaluated at the optimal geometry of the lowest excited state S_1, $\left(\{\boldsymbol{Q}_i\}, (i = 1, \dots, 3N-6)\right)$

$$\boldsymbol{d}_{12}^{SVD,k} = \sum_{i=1}^{3N-6} c_i \mathbf{Q}_i \,, (k = 1,2, \dots), \qquad (5)$$

with $c_i = \boldsymbol{d}_{12}^{SVD,k} \cdot \boldsymbol{Q}_i$.

Besides, the vibrational kinetic energy $K_i(t)$ associated with a given ENM $\mathbf{Q}_i$ is calculated using the corresponding velocities $\dot{\boldsymbol{Q}}_i$ as

$$K_i(t) = \left(\dot{\boldsymbol{Q}}_i(t)\right)^2, \qquad (6)$$

and the corresponding total vibrational energy is obtained from the virial theorem, $E_i(t) = 2K_i(t)$. More details on this approach can be found elsewhere.[22]

NOTES

The authors declare no competing financial interest. The Non-adiabatic EXcited state molecular dynamics (NEXMD) Program code, license, and documentation may be accessed at https://github.com/lanl/NEXMD .

ACKNOWLEDGEMENTS

A.M. and S.S. acknowledge financial support from the National Science Foundation (NSF) CAREER program, under grant number DMR-1847774. This research used resources provided by the LANL Institutional Computing Program and the Boston University Shared Computing Cluster. This work was partially supported by CONICET, UNQ, ANPCyT (PICT-2018-2360). The work at Los Alamos National Laboratory (LANL) was supported by the LANL Directed Research and Development Funds (LDRD) and performed in part at the Center for Center for Integrated Nanotechnologies (CINT), a U.S. Department of Energy, Office of Science User Facility.

SUPPORTING INFORMATION

Supporting information contains transition densities of monomers, dimers and trimer; comparison of absorption spectra calculated with different levels of theory; Frenkel exciton model for perylene diimide dimer and trimer; excited state energies of dimers and trimer; comparison of average absolute values of the non-adiabatic coupling terms for monomer, dimer and trimer; dimer's and trimer's active normal modes; the localization of the TD for the dimer, trimer and dimer with backbone; figures of impact of the backbone on absorption spectrum of dimer; comparison of average absolute values of the non-adiabatic coupling terms for monomer and dimer molecules with and without backbone; comparison of average absolute values of the non-adiabatic coupling terms for dimer and dimer with backbone; comparison of population dynamics for three dimer cases.

REFERENCES:

(1) Laquai, F.; Park, Y.-S.; Kim, J.-J.; Basché, T. Excitation Energy Transfer in Organic Materials: From Fundamentals to Optoelectronic Devices. *Macromol. Rapid Commun.* **2009**, *30* (14), 1203–1231. https://doi.org/10.1002/marc.200900309.

(2) Scholes, G. D.; Fleming, G. R.; Olaya-Castro, A.; van Grondelle, R. Lessons from Nature about Solar Light Harvesting. *Nat. Chem.* **2011**, *3* (10), 763–774. https://doi.org/10.1038/nchem.1145.

(3) Kippelen, B.; Brédas, J. L. Organic Photovoltaics. *Energy Environ. Sci.* **2009**, *2* (3), 251–261. https://doi.org/10.1039/b812502n.

(4) Jiang, Y.; McNeill, J. Light-Harvesting and Amplified Energy Transfer in Conjugated Polymer Nanoparticles. *Chem. Rev.* **2017**, *117* (2), 838–859. https://doi.org/10.1021/acs.chemrev.6b00419.

(5) Saga, Y.; Yamashita, M.; Masaoka, Y.; Hidaka, T.; Imanishi, M.; Kimura, Y.; Nagasawa, Y. Excitation Energy Transfer from Bacteriochlorophyll b in the B800 Site to B850

Bacteriochlorophyll a in Light-Harvesting Complex 2. *J. Phys. Chem. B* **2021**, *125* (8). https://doi.org/10.1021/acs.jpcb.0c09605.
(6) Otsuki, J. Supramolecular Approach towards Light-Harvesting Materials Based on Porphyrins and Chlorophylls. *J. Mater. Chem. A* **2018**, *6* (16). https://doi.org/10.1039/c7ta11274b.
(7) Proppe, A. H.; Li, Y. C.; Aspuru-Guzik, A.; Berlinguette, C. P.; Chang, C. J.; Cogdell, R.; Doyle, A. G.; Flick, J.; Gabor, N. M.; van Grondelle, R.; Hammes-Schiffer, S.; Jaffer, S. A.; Kelley, S. O.; Leclerc, M.; Leo, K.; Mallouk, T. E.; Narang, P.; Schlau-Cohen, G. S.; Scholes, G. D.; Vojvodic, A.; Yam, V. W. W.; Yang, J. Y.; Sargent, E. H. Bioinspiration in Light Harvesting and Catalysis. *Nature Reviews Materials*. 2020. https://doi.org/10.1038/s41578-020-0222-0.
(8) Bennett, D. I. G.; Amarnath, K.; Fleming, G. R. A Structure-Based Model of Energy Transfer Reveals the Principles of Light Harvesting in Photosystem II Supercomplexes. *J. Am. Chem. Soc.* **2013**, *135* (24). https://doi.org/10.1021/ja403685a.
(9) Feron, K.; Belcher, W. J.; Fell, C. J.; Dastoor, P. C. Organic Solar Cells: Understanding the Role of F̈orster Resonance Energy Transfer. *International Journal of Molecular Sciences*. 2012. https://doi.org/10.3390/ijms131217019.
(10) Roy, P. P.; Kundu, S.; Valdiviezo, J.; Bullard, G.; Fletcher, J. T.; Liu, R.; Yang, S.-J.; Zhang, P.; Beratan, D. N.; Therien, M. J.; Makri, N.; Fleming, G. R. Synthetic Control of Exciton Dynamics in Bioinspired Cofacial Porphyrin Dimers. *J. Am. Chem. Soc.* **2022**. https://doi.org/10.1021/jacs.1c12889.
(11) Wirsing, S.; Hänsel, M.; Belova, V.; Schreiber, F.; Broch, K.; Engels, B.; Tegeder, P. Excited-State Dynamics in Perylene-Based Organic Semiconductor Thin Films: Theory Meets Experiment. *J. Phys. Chem. C* **2019**, *123* (45), 27561–27572. https://doi.org/10.1021/acs.jpcc.9b07511.
(12) Haedler, A. T.; Kreger, K.; Issac, A.; Wittmann, B.; Kivala, M.; Hammer, N.; Köhler, J.; Schmidt, H. W.; Hildner, R. Long-Range Energy Transport in Single Supramolecular Nanofibres at Room Temperature. *Nature* **2015**, *523* (7559), 196–199. https://doi.org/10.1038/nature14570.
(13) Chaudhuri, D.; Li, D.; Che, Y.; Shafran, E.; Gerton, J. M.; Zang, L.; Lupton, J. M. Enhancing Long-Range Exciton Guiding in Molecular Nanowires by H-Aggregation Lifetime Engineering. *Nano Lett.* **2011**, *11* (2), 488–492. https://doi.org/10.1021/nl1033039.
(14) Chenu, A.; Scholes, G. D. Coherence in Energy Transfer and Photosynthesis. *Annu. Rev. Phys. Chem.* **2015**, *66* (August), 69–96. https://doi.org/10.1146/annurev-physchem-040214-121713.
(15) Mirkovic, T.; Ostroumov, E. E.; Anna, J. M.; Van Grondelle, R.; Govindjee; Scholes, G. D. Light Absorption and Energy Transfer in the Antenna Complexes of Photosynthetic Organisms. *Chem. Rev.* **2017**, *117* (2), 249–293. https://doi.org/10.1021/acs.chemrev.6b00002.
(16) Delor, M.; Dai, J.; Roberts, T. D.; Rogers, J. R.; Hamed, S. M.; Neaton, J. B.; Geissler, P. L.; Francis, M. B.; Ginsberg, N. S. Exploiting Chromophore-Protein Interactions through Linker Engineering to Tune Photoinduced Dynamics in a Biomimetic Light-Harvesting Platform. *J. Am. Chem. Soc.* **2018**, *140* (20). https://doi.org/10.1021/jacs.7b13598.
(17) Chen, H.; Zong, X. L.; Song, W.; Li, D. C.; Cao, Z. L. Vibration-Assisted Light Absorption and Excitation Energy Transfer in Photosynthetic Processes. *Quantum Inf.*

Process. **2021**, *20* (9), 1–11. https://doi.org/10.1007/s11128-021-03207-9.
(18) Franck, J. Elementary Processes of Photochemical Reactions. *Trans. Faraday Soc.* **1926**, *21* (FEBRUARY). https://doi.org/10.1039/TF9262100536.
(19) Hestand, N. J.; Spano, F. C. Expanded Theory of H- and J-Molecular Aggregates: The Effects of Vibronic Coupling and Intermolecular Charge Transfer. *Chem. Rev.* **2018**, *118* (15), 7069–7163. https://doi.org/10.1021/acs.chemrev.7b00581.
(20) Bricker, W. P.; Shenai, P. M.; Ghosh, A.; Liu, Z.; Enriquez, M. G. M.; Lambrev, P. H.; Tan, H. S.; Lo, C. S.; Tretiak, S.; Fernandez-Alberti, S.; Zhao, Y. Non-Radiative Relaxation of Photoexcited Chlorophylls: Theoretical and Experimental Study. *Sci. Rep.* **2015**, *5*, 1–16. https://doi.org/10.1038/srep13625.
(21) Nelson, T. R.; Ondarse-Alvarez, D.; Oldani, N.; Rodriguez-Hernandez, B.; Alfonso-Hernandez, L.; Galindo, J. F.; Kleiman, V. D.; Fernandez-Alberti, S.; Roitberg, A. E.; Tretiak, S. Coherent Exciton-Vibrational Dynamics and Energy Transfer in Conjugated Organics. *Nat. Commun.* **2018**, *9* (1), 2316. https://doi.org/10.1038/s41467-018-04694-8.
(22) Alfonso-Hernandez, L.; Athanasopoulos, S.; Tretiak, S.; Miguel, B.; Bastida, A.; Fernandez-Alberti, S. Vibrational Energy Redistribution during Donor–Acceptor Electronic Energy Transfer: Criteria to Identify Subsets of Active Normal Modes. *Phys. Chem. Chem. Phys.* **2020**, *22* (33), 18454–18466. https://doi.org/10.1039/D0CP03102J.
(23) Han, Y.; Zhang, X.; Ge, Z.; Gao, Z.; Liao, R.; Wang, F. A Bioinspired Sequential Energy Transfer System Constructed via Supramolecular Copolymerization. *Nat. Commun.* **2022**, *13* (1), 1–10. https://doi.org/10.1038/s41467-022-31094-w.
(24) Würthner, F. Perylene Bisimide Dyes as Versatile Building Blocks for Functional Supramolecular Architectures. *Chem. Commun.* **2004**, *4* (14), 1564–1579. https://doi.org/10.1039/b401630k.
(25) Huang, C.; Barlow, S.; Marder, S. R. Perylene-3,4,9,10-Tetracarboxylic Acid Diimides: Synthesis, Physical Properties, and Use in Organic Electronics. *Journal of Organic Chemistry*. 2011, pp 2386–2407. https://doi.org/10.1021/jo2001963.
(26) Idé, J.; Méreau, R.; Ducasse, L.; Castet, F.; Olivier, Y.; Martinelli, N.; Cornil, J.; Beljonne, D. Supramolecular Organization and Charge Transport Properties of Self-Assembled π-π Stacks of Perylene Diimide Dyes. *J. Phys. Chem. B* **2011**, *115* (18), 5593–5603. https://doi.org/10.1021/jp111422v.
(27) May, F.; Marcon, V.; Hansen, M. R.; Grozema, F.; Andrienko, D. Relationship between Supramolecular Assembly and Charge-Carrier Mobility in Perylenediimide Derivatives: The Impact of Side Chains. *J. Mater. Chem.* **2011**, *21* (26), 9538–9545. https://doi.org/10.1039/c1jm10500k.
(28) Chiş, V.; Mile, G.; Ştiufiuc, R.; Leopold, N.; Oltean, M. Vibrational and Electronic Structure of PTCDI and Melamine-PTCDI Complexes. *J. Mol. Struct.* **2009**, *924–926* (C), 47–53. https://doi.org/10.1016/j.molstruc.2008.12.038.
(29) Oltean, M.; Calborean, A.; Mile, G.; Vidrighin, M.; Iosin, M.; Leopold, L.; Maniu, D.; Leopold, N.; Chiş, V. Absorption Spectra of PTCDI: A Combined UV-Vis and TD-DFT Study. *Spectrochim. Acta - Part A Mol. Biomol. Spectrosc.* **2012**, *97*, 703–710. https://doi.org/10.1016/j.saa.2012.07.056.
(30) Clark, A. E.; Qin, C.; Li, A. D. Q. Beyond Exciton Theory: A Time-Dependent DFT and Franck-Condon Study of Perylene Diimide and Its Chromophoric Dimer. *J. Am. Chem. Soc.* **2007**, *129* (24), 7586–7595. https://doi.org/10.1021/ja0687724.
(31) Hestand, N. J.; Spano, F. C. Molecular Aggregate Photophysics beyond the Kasha Model:

Novel Design Principles for Organic Materials. *Acc. Chem. Res.* **2017**, *50* (2), 341–350. https://doi.org/10.1021/acs.accounts.6b00576.
(32) Mukazhanova, A.; Trerayapiwat, K. J.; Mazaheripour, A.; Wardrip, A. G.; Frey, N. C.; Nguyen, H.; Gorodetsky, A. A.; Sharifzadeh, S. Accurate First-Principles Calculation of the Vibronic Spectrum of Stacked Perylene Tetracarboxylic Acid Diimides. *J. Phys. Chem. A* **2020**, *124* (16), 3055–3063. https://doi.org/10.1021/acs.jpca.9b08117.
(33) Kumar, M.; Provazza, J.; Coker, D. F. Influence of Solution Phase Environmental Heterogeneity and Fluctuations on Vibronic Spectra: Perylene Diimide Molecular Chromophore Complexes in Solution. *J. Chem. Phys.* **2021**, *154* (22). https://doi.org/10.1063/5.0054377.
(34) Huang, T.; Lewis, D. K.; Sharifzadeh, S. Assessing the Role of Intermolecular Interactions in a Perylene-Based Nanowire Using First-Principles Many-Body Perturbation Theory. *J. Phys. Chem. Lett.* **2019**, *10* (11), 2842–2848. https://doi.org/10.1021/acs.jpclett.9b00800.
(35) Gao, F.; Zhao, Y.; Liang, W. Vibronic Spectra of Perylene Bisimide Oligomers: Effects of Intermolecular Charge-Transfer Excitation and Conformational Flexibility. *J. Phys. Chem. B* **2011**, *115* (12), 2699–2708. https://doi.org/10.1021/jp107449v.
(36) Pan, F.; Gao, F.; Liang, W.; Zhao, Y. Nature of Low-Lying Excited States in H-Aggregated Perylene Bisimide Dyes: Results of TD-LRC-DFT and the Mixed Exciton Model. *J. Phys. Chem. B* **2009**, *113* (44), 14581–14587. https://doi.org/10.1021/jp9061972.
(37) Seibt, J.; Winkler, T.; Renziehausen, K.; Dehm, V.; Würthner, F.; Meyer, H. D.; Engel, V. Vibronic Transitions and Quantum Dynamics in Molecular Oligomers: A Theoretical Analysis with an Application to Aggregates of Perylene Bisimides. *J. Phys. Chem. A* **2009**, *113* (48), 13475–13482. https://doi.org/10.1021/jp904892v.
(38) Ma, L.; Tan, K. J.; Jiang, H.; Kloc, C.; Michel-Beyerle, M. E.; Gurzadyan, G. G. Excited-State Dynamics in an α-Perylene Single Crystal: Two-Photon- and Consecutive Two-Quantum-Induced Singlet Fission. *J. Phys. Chem. A* **2014**, *118* (5), 838–843. https://doi.org/10.1021/jp409977f.
(39) Segalina, A.; Assfeld, X.; Monari, A.; Pastore, M. Computational Modeling of Exciton Localization in Self-Assembled Perylene Helices: Effects of Thermal Motion and Aggregate Size. *J. Phys. Chem. C* **2019**, *123* (11), 6427–6437. https://doi.org/10.1021/acs.jpcc.9b00494.
(40) Mukazhanova, A.; Malone, W.; Negrin-Yuvero, H.; Fernandez-Alberti, S.; Tretiak, S.; Sharifzadeh, S. Photoexcitation Dynamics in Perylene Diimide Dimers. *J. Chem. Phys.* **2020**, *153* (24), 244117. https://doi.org/10.1063/5.0031485.
(41) Negrin-Yuvero, H.; Mukazhanova, A.; Freixas, V. M.; Tretiak, S.; Sharifzadeh, S.; Fernandez-Alberti, S. Vibronic Photoexcitation Dynamics of Perylene Diimide: Computational Insights. *J. Phys. Chem. A* **2022**, *126* (5). https://doi.org/10.1021/acs.jpca.1c09484.
(42) Malone, W.; Nebgen, B.; White, A.; Zhang, Y.; Song, H.; Bjorgaard, J. A.; Sifain, A. E.; Rodriguez-Hernandez, B.; Freixas, V. M.; Fernandez-Alberti, S.; Roitberg, A. E.; Nelson, T. R.; Tretiak, S. NEXMD Software Package for Nonadiabatic Excited State Molecular Dynamics Simulations. *J. Chem. Theory Comput.* **2020**, *16* (9), 5771–5783. https://doi.org/10.1021/acs.jctc.0c00248.
(43) Pope, M.; Swenberg, C. E. *Electronic Processes in Organic Crystals and Polymers*; 1999.

(44) Nelson, T.; Fernandez-Aberti, S.; Chernyak, V.; Roitberg, A. E.; Tretiak, S. Nonadiabatic Excited-State Molecular Dynamics Modeling of Photoinduced Dynamics in Conjugated Molecules. *J. Phys. Chem. B* **2011**, *115* (18), 5402–5414. https://doi.org/10.1021/jp109522g.

(45) Reimers, J. R.; Biczysko, M.; Bruce, D.; Coker, D. F.; Frankcombe, T. J.; Hashimoto, H.; Hauer, J.; Jankowiak, R.; Kramer, T.; Linnanto, J.; Mamedov, F.; Müh, F.; Rätsep, M.; Renger, T.; Styring, S.; Wan, J.; Wang, Z.; Wang-Otomo, Z.-Y.; Weng, Y.-X.; Yang, C.; Zhang, J.-P.; Freiberg, A.; Krausz, E. Challenges Facing an Understanding of the Nature of Low-Energy Excited States in Photosynthesis. *Biochim. Biophys. Acta - Bioenerg.* **2016**, *1857* (9), 1627–1640. https://doi.org/10.1016/j.bbabio.2016.06.010.

(46) Chai, J. Da; Head-Gordon, M. Long-Range Corrected Hybrid Density Functionals with Damped Atom-Atom Dispersion Corrections. *Phys. Chem. Chem. Phys.* **2008**, *10* (44), 6615–6620. https://doi.org/10.1039/b810189b.

(47) Frisch, M. J.; Trucks, G. W.; Schlegel, H. E.; Scuseria, G. E.; Robb, M. A.; Cheeseman, J. R.; Scalmani, G.; Barone, V.; Petersson, G. A.; O., F.; Foresman, J. B.; Fox, J. D. Gaussian 16. *Gaussian, Inc., Wallingford CT,*. Gaussian, Inc., Wallingford CT, 2016 2016.

(48) Dewar, M. J. S.; Zoebisch, E. G.; Healy, E. F.; Stewart, J. J. P. Development and Use of Quantum Mechanical Molecular Models. 76. AM1: A New General Purpose Quantum Mechanical Molecular Model. *J. Am. Chem. Soc.* **1985**, *107* (13). https://doi.org/10.1021/ja00299a024.

(49) Dewar, M. J. S.; Zoebisch, E. G.; Healy, E. F.; Stewart, J. J. P. AM1: A New General Purpose Quantum Mechanical Molecular Model1. *J. Am. Chem. Soc.* **1985**, *107* (13), 3902–3909. https://doi.org/10.1021/ja00299a024.

(50) Andersen, H. C. Rattle: A "Velocity" Version of the Shake Algorithm for Molecular Dynamics Calculations. *J. Comput. Phys.* **1983**, *52* (1), 24–34. https://doi.org/10.1016/0021-9991(83)90014-1.

(51) Nelson, T.; Fernandez-Alberti, S.; Roitberg, A. E.; Tretiak, S. Nonadiabatic Excited-State Molecular Dynamics: Treatment of Electronic Decoherence. *J. Chem. Phys.* **2013**, *138* (22), 224111. https://doi.org/10.1063/1.4809568.

(52) Fernandez-Alberti, S.; Roitberg, A. E.; Nelson, T.; Tretiak, S. Identification of Unavoided Crossings in Nonadiabatic Photoexcited Dynamics Involving Multiple Electronic States in Polyatomic Conjugated Molecules. *J. Chem. Phys.* **2012**, *137* (1), 014512. https://doi.org/10.1063/1.4732536.

(53) Dimitriev, O. Dynamics of Excitons in Conjugated Molecules and Organic Semiconductor Systems. *Chem. Rev.* **2022**, 122 (9), 8487-8593. https://doi.org/10.1021/acs.chemrev.1c00648